ISSN 1330-3651 (Print), ISSN 1848-6339 (Online) https://doi.org/10.17559/TV-20250106002239
Original scientific paper

Design of Pneumatic Conveying Device for Straw Micro-Crusher Based on CFD-DEM Simulation

Min FU*, Lei CHEN, Zhong CAO, Mingyu ZHAN, Zijian WANG

Abstract: To solve the problem that the complexity of the internal airflow field of the machine leads to low conveying capacity and affects the crushing and classifying performance of the impact crusher in the process of straw micro-crushing, conveying and classifying, a straw micro-crusher pneumatic conveying device is designed. Based on the force analysis of straw in the conveying channel, this study combines theoretical calculations and numerical simulations to determine the suspension velocity of straw particle, conveying airflow velocity, and volumetric flow rate in pneumatic conveying. Simulation experiments are carried out using the coupled Computational Fluid Dynamics-Discrete Element Method (CFD-DEM) to investigate the airflow distribution patterns and the motion characteristics of straw particles in the process of pneumatic conveying, to clarify the key parameters affecting the conveying efficiency, to determine the optimal values of the key parameters - air inlet width, inlet airflow velocity and flow deflector diameter by the single-factor experiments. A prototype is manufactured, and the relative error in conveying capacity is regarded as an evaluation index to carry out conveying performance tests of pneumatic conveying device. The test results verify the reasonableness of the structural design of the conveying device and the correctness of the theoretical calculations and CFD-DEM coupled simulation results. The findings of this study provide a reference for the design of efficient pneumatic conveying equipment for biomass powder.

Keywords: airflow distribution; conveying performance; powder; suspension velocity

1 INTRODUCTION

Crop straw refers to the residual parts of crops such as corn, rice, wheat, cotton, and sugarcane after harvest. It is mainly composed of cellulose, hemicellulose, and lignin and is a renewable energy source [1]. Straw powder obtained through micro-crushing has advantages such as fine particle size, high purity, narrow size distribution, uniform quality, and increased specific surface area. It can be used as a new energy-saving and environmentally friendly material in applications such as biodegradable mulch, innovative cushioning and packaging materials, lightweight building materials [2, 3], and household products [4]. These applications enable the high-value utilization of straw, moving beyond low-value-added areas such as heating and feed, thereby achieving the goals of resource conservation and environmental protection [5]. The market demand for straw powder is increasing, but currently, there is a lack of micro-crushing equipment capable of large-scale production for straw, with equipment designed for minerals and medicinal herbs often being used as substitutes [6].

Impact crusher features the advantages of large crushing ratio, adjustable particle size, simple structure, large capacity and high efficiency, and is widely used in the field of micro-crushing of heat-sensitive materials and fibrous materials such as chemical raw materials, rubber, traditional Chinese medicine, and feed. It can also be used for the production of ultrafine powder from medium-hardness materials, such as calcite, marble, chalk, and talc [7]. However, there are problems such as bad adaptability of raw materials, large particle size and low crushing efficiency when the impact crusher is applied to straw micro-crushing. The impact crusher crushes materials through the intense impact of elements installed on the rotor (such as hammers, blades, cutters, or rods). Under the dual action of air vortices and centrifugal force, the materials experience mutual collisions as well as strong shearing, grinding, and impacting with the rotor. This process crushes the materials, which are subsequently transported by airflow to the classification zone for separation and screening [8]. However, the impact crushers currently available on the market lack an independent pneumatic conveying system. Material conveying, crushing, and classification occur within the same chamber, where the complex mixed airflow field generated in the crushing and classification zones interferes with the normal conveying of materials and affects the crushing and classification performance.

To address the aforementioned issues, our research team proposes a novel design scheme for a straw micro-crusher. Unlike previous studies that focused on optimizing internal components to improve conveying efficiency, this study introduces an innovative structural design of the micro-crusher. It adopts an independent pneumatic conveying channel to separate the processes of straw crushing, classifying, and conveying, thereby avoiding the negative effects of mixed airflow fields on straw micro-crushing and classifying. The present powder pneumatic conveying technology utilizes airflow with certain pressure and velocity to convey powder materials in a pipe with a fixed structural shape [9], which is mostly applied in chemical [10, 11], food [12], pharmaceutical [13], mineral processing [14], construction [15] and other industries. Researches on pneumatic conveying of biomass straw focus on large straw particles after coarse crushing [16, 17], while there are few studies on pneumatic conveying devices and conveying technologies for straw powder after micro-crushing.

Due to the difficulty in observing the pneumatic conveying process and the complexity of the flow field, most researchers rely on simulation methods to study the pneumatic conveying of powders. Lu et al. [18] used the numerical simulation method of Computational Particle Fluid Dynamics (CPFD) to study the conveying characteristics and airflow patterns of pulverized coal in vertical conveying channels under different superficial gas velocities. The simulation results showed that the gas-solid two-phase flow of pulverized coal in the conveying channel exhibited full-pipe flow, annular flow, and

suspension flow sequentially as the airflow velocity increased. Pneumatic conveying experiments confirmed the accuracy of the numerical simulation results. Zhou et al. [19] utilized the CFD-DEM coupled numerical simulation method to investigate the motion characteristics of particles in pneumatic conveying within vertical pipelines. The results indicated that the airflow patterns in the pipe transitioned sequentially from high-concentration core-annular flow, to medium-concentration core-annular flow, to low-concentration core-annular flow, and finally to suspension flow as the gas velocity increased, with the cross-sectional particle volume fraction gradually decreasing. Song et al. [20] numerically simulated the characteristics of dilute-phase airflow transport of feed particles based on a coupled CFD-DEM method, and found that the vertical duct pressure drop showed a tendency to decline and then rise with the increase in inlet air velocity. Chen et al. [21] investigated the gas-solid two-phase flow of rigid shotcrete during horizontal pneumatic conveying through tests, revealed the flow characteristics of rigid shotcrete in horizontal pipelines, and analyzed the unit pressure drop and particle flow characteristics of the steady state zone of rigid shotcrete under different airflow rates, water-cement ratios and pipe diameters with a pressure transmitter and high-speed camera system. Wang et al. [22] developed computational fluid and discrete element models based on Computational Fluid Dynamics (CFD) and Discrete Element Method (DEM). Through numerical simulation of gas-solid two-phase flow, they found that conveying air velocity has the greatest impact on pneumatic conveying. Higher air velocities shorten the time for particles to achieve dynamic stability, improving conveying efficiency but also increasing power consumption correspondingly. The above studies provide valuable references for the research on pneumatic conveying of biomass straw powder.

To meet the requirements of the actual conveying capacity of straw powder, this paper carries out the design and test research on the pneumatic conveying device based on the design requirements of straw micro-crusher. Based on force analysis of straw in the conveying channel, a combination of theoretical calculations and numerical simulations is used to determine the suspension velocity of straw particle, conveying airflow velocity, and volumetric flow rate. The simulation experiment is conducted using the CFD-DEM coupling method to investigate the airflow distribution patterns and the motion characteristics of straw particles during the conveying process, analyze the key parameters influencing the conveying efficiency, and determine the optimal values of the key parameters by the single-factor experiments. A prototype is manufactured, and conveying performance test of the pneumatic conveying device is carried out with corn straw as the test object to verify the reasonableness of the structure of the conveying device, and the correctness of the theoretical calculations and the results of the CFD-DEM coupled simulation.

2 METHODS AND EXPERIMENTAL

2.1 Overall Structure and Working Principle

This research team proposes a novel design scheme for straw micro-crusher, which simultaneously achieves straw crushing, conveying, and classifying operations. Its structure, as shown in Fig. 1, mainly consists of crushing device, classifying device, pneumatic conveying device, screw conveyor and support base. The crushing device is located at the center of the machine and includes crushing movable cutters, crushing fixed cutters, crushing hood, crushing chamber and crushing motor. Its primary function is to micronize the straw. The classifying device is located at the top of the machine and mainly comprises classifying motor, flow duiding loop, rotor cage and classifying chamber. Its function is to classify the micronized straw powder. The pneumatic conveying device is situated on the exterior of the crushing and classifying device. It consists of ventilators, air inlets, air storage chamber, flow deflector, conveying channel and fine powder outlet to transport the micronized straw. The main technical parameters of the straw micro-crusher are shown in Tab. 1.

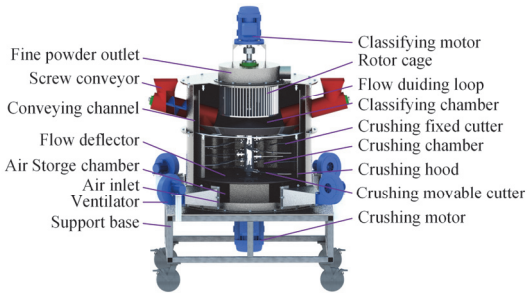

Figure 1 The straw micro-crusher

Table 1 Main technical parameters of the straw micro-crusher

Parameters	Values
Equipment dimensions (L × H × W) / mm × mm × mm	1400 × 1400 × 2000
Maximum rotational speed of the crusher main shaft / r/min	2800
Maximum rotational speed of the classifier shaft / r/min	2800
The power of the crushing motor / kW	7.5
The power of the classifying motor / kW	3.0
Volumetric flow rate / m³/h	4300
Inlet airflow velocity / m/s	8.4
Output / kg/h	600
The power of the ventilator / kW	0.75 × 4
Feeding particle size / mm	5-15
Discharge particle size / μm	40-60
Conveying capacity / kg/h	750

Working principle: After pretreatment, corn straw (particle size of 5-15 mm, moisture content of 15-25%) is fed into the crushing device by the screw conveyor. It is crushed under the impact and shearing action of the crushing movable and fixed cutters, and then falls onto the flow deflector at the bottom of the crushing chamber. Under the negative pressure generated by the rotary airflow and the airflow in the conveying channel, the straw is transported along the circular pneumatic conveying channel to the classifying device. Straw powder meeting the particle size requirements is discharged through the fine powder outlet, while oversized powder returns to the crushing device for further crushing.

2.2 Structural Parameters Design of Pneumatic Conveying Device

As shown in Fig. 2a, the pneumatic conveying device mainly consists of ventilators, air inlets, air storage

chamber, flow deflector, conveying channel, and fine powder outlet. The ventilators generate airflow to provide conveying power for the device, and the airflow velocity can be adjusted as needed. The air inlets are located at the lower part of the conveying device. To maintain the stability of the airflow field in the air storage chamber and conveying channel and ensure uniform straw transport, four air inlets are evenly distributed along the circumference. The air storage chamber, located at the bottom of the conveying device, stores the horizontal airflow from the air inlets and provides sufficient airflow for the conveying channel. The flow deflector, positioned above the air storage chamber, separates the storage chamber from the crushing chamber and guides the airflow into the conveying channel. The conveying channel is located in the middle of the device. It is an annular channel formed by the outer wall of the crushing hood, the outer wall of the flow duiding loop, and the inner wall of the housing. It uses vertical airflow to transport the crushed straw. The fine powder outlet, located at the top of the conveying device, discharges straw powder that meets the required particle size. The airflow path inside the pneumatic conveying device is shown in Fig. 2b.

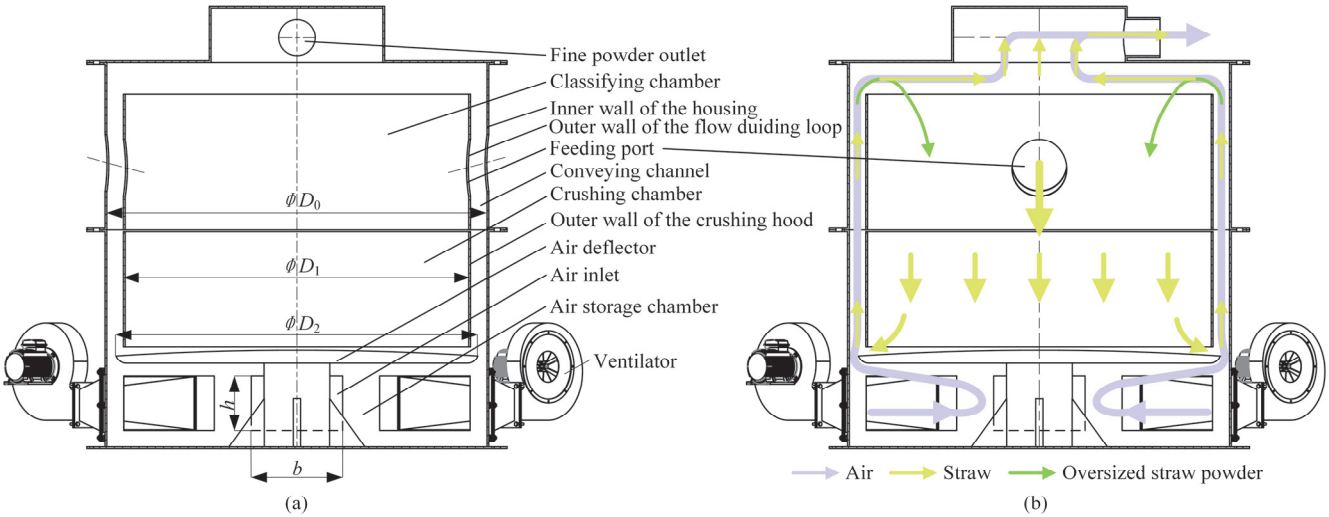

Figure 2 Structure and airflow path of the pneumatic conveying device: (a) Structure of pneumatic conveying device; (b) Airflow path

To ensure adequate air intake, the air inlet height h of the pneumatic conveying device must not exceed the height of the air storage chamber, which is set at 150 mm [23]. The air inlet width b will be determined later through single-factor simulation experiment. The inner diameter D_1 of the conveying channel measures 950 mm. The outer diameter D_0 of the conveying channel is established at 1050 mm, based on the overall dimensions and conveying capacity of the pneumatic conveying device. From Fig. 2a, it can be seen that the flow deflector diameter D_2 is between the inner diameter D_1 and outer diameter D_0 of the conveying channel. Thus, the range of flow deflector diameter is between 950 mm and 1050 mm, and its exact value will be determined later through one-factor simulation test analysis.

The conveying channel's cross-section designed in this paper is annular, and the equivalent diameter of a circle with the same area is calculated using Eq. (1).

$$\pi\left(\frac{D_0}{2}\right)^2-\pi\left(\frac{D_1}{2}\right)^2=\pi\left(\frac{D}{2}\right)^2 \tag{1}$$

where: D_0 is the outer diameter of the conveying channel / mm, D_1 is the inner diameter of the conveying channel / mm, D is the equivalent diameter of the conveying channel / mm.

The equivalent diameter D of the conveying channel is 450 mm obtained from Eq. (1).

2.3 Working Parameters Design of Pneumatic Conveying Device

The suspension velocity of straw particle, conveying airflow velocity, and volumetric flow rate are essential working parameters of a pneumatic conveying device [24, 25]. The suspension velocity of straw particle refers to the minimum airflow velocity required to keep straw particle suspended within a vertical pipeline. Both the conveying airflow velocity and volumetric flow rate are derived from this suspension velocity. It is significant to select the values of these two parameters appropriately to reduce the energy loss in the pneumatic conveying device and improve the straw conveying capacity [26].

2.3.1 Suspension Velocity of Straw Particle

In the process of conveying, the straw particle is subjected to gravity G, buoyancy F_B, and aerodynamic drag F_D. For the convenience of the study, it is assumed that the straw particle is spherical, gnoring interactions between straw particles. Meanwhile, considering the actual transportation of straw particle in the conveying channel, the study of suspension velocity is carried out with a vertical pipe. In the vertical pneumatic conveying channel, as shown in Fig. 3, the straw particle moves upward from the bottom of the pipe under the action of airflow. As the relative velocity between straw particle and airflow increases, the aerodynamic drag also rises. Eventually, the straw particle reaches equilibrium under the buoyancy F_B

and aerodynamic drag F_D and gravity G, attaining a suspended state [27].

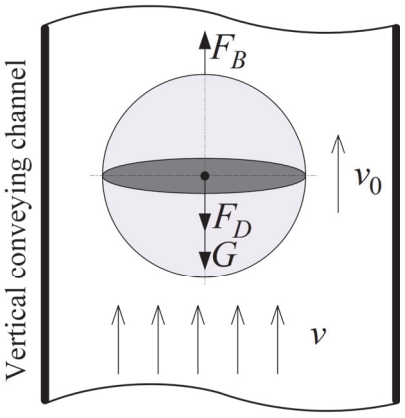

Figure 3 Force analysis of strawparticle

The expressions for F_B, F_D, and G are given in Eq. (2) to Eq. (4) [28].

$$F_B = \frac{1}{6}\pi d_s^3 \rho g \tag{2}$$

$$F_D = \frac{\pi C}{8} d_s^2 \rho v_0^2 \tag{3}$$

$$G = \frac{1}{6}\pi d_s^3 \rho_s g \tag{4}$$

Straw particle in equilibrium suspension satisfies $F_B = G + F_D$.

$$\frac{\pi C}{8} d_s^2 \rho v_0^2 = \frac{\pi}{6} d_s^3 (\rho_s - \rho) g \tag{5}$$

From Eq. (5), the equation for the suspension velocity of straw particle is derived as:

$$v_0 = \sqrt{\frac{4 g d_s (\rho_s - \rho)}{3 C \rho}} \tag{6}$$

where: G is gravity / N, F_B is buoyancy / N, F_D is aerodynamic drag / N, d_s is the equivalent diameter of straw particle / m, ρ_s is the density of straw particle / kg/m^3, g is the acceleration of gravity / m/s^2, ρ is the air density / kg/m^3, C is the drag coefficient, v_0 is the suspension velocity of straw particle / m/s.

The drag coefficient C is a function of the Reynolds number Re. The drag coefficient is determined using the partitioned suspension velocity formula and corresponding particle size applicability method according to the equivalent particle diameter range of the material [28], where $C = 0.44$.

There are two kinds of motion states, laminar flow and turbulent flow, in the straw particle conveying channel. The state of flow of the straw particles in the conveying channel is determined by the value of the Reynolds coefficient. Eq. (8) is the Reynolds factor calculation formula.

$$C = \begin{cases} \dfrac{24}{R_e} & \left(d_s \le 2.2\left[\dfrac{\mu^2}{\rho(\rho_s - \rho)}\right]^{\frac{1}{3}} \right) \\ \dfrac{10}{\sqrt{R_e}} & \left(2.2\left[\dfrac{\mu^2}{\rho(\rho_s - \rho)}\right]^{\frac{1}{3}} < d_s \le 20.4\left[\dfrac{\mu^2}{\rho(\rho_s - \rho)}\right]^{\frac{1}{3}} \right) \\ 0.44 & \left(20.4\left[\dfrac{\mu^2}{\rho(\rho_s - \rho)}\right]^{\frac{1}{3}} < d_s \le 1100\left[\dfrac{\mu^2}{\rho(\rho_s - \rho)}\right]^{\frac{1}{3}} \right) \end{cases} \tag{7}$$

$$R_e = \frac{v_0 D \rho}{\mu} \tag{8}$$

where: μ is the aerodynamic viscosity / Pa·s.

The effect of the pipe wall on the state of motion of irregular straw particle is considered, as well as the presence or absence of rotation around the center of gravity in the motion of the particle. The calculation of the suspension velocity of pneumatically conveyed non-spherical straw particle in the vertical conveying channel is usually corrected by converting irregularly shaped straw particle into equivalent sphere and using the diameter d_s of the equivalent sphere as the diameter of the irregular particle [29].

$$v_1 = \sqrt{\frac{4 g d_s (\rho_s - \rho)}{3 C \rho}} \left[1 - \left(\frac{d_s}{D} \right)^2 \right] \tag{9}$$

$$d_s = 1.24 \left(\frac{m}{\rho_s} \right)^{\frac{1}{3}} \tag{10}$$

where: v_1 is the suspension velocity of non-spherical straw particle / m/s; m is the mass of straw particle / kg, D is the equivalent diameter of the conveying channel / m.

The drag coefficient of irregularly shaped straw material particle is larger than the drag coefficient of spherical particle, and the shape of material particle has a greater effect on the suspension velocity. Considering the effect of particle shape, the suspension velocity is corrected by Eq. (11):

$$v_{xm} = \frac{v_1}{\sqrt{k_x}} \tag{11}$$

where: v_{xm} is the corrected suspension velocity of straw particle / m/s, k_x is the correction coefficient (the value is related to the size of the straw particle).

After the straw is crushed, the particles in the particle cluster vary in size. It is clear from Eq. (5) that if the large volume of straw particle can be properly pneumatically conveyed, then the small volume of straw particle can also be properly conveyed. Maximum feed size is taken in this paper in order to simplify the calculation process and reduce the difficulty of subsequent simulation. In the

calculation, g is 9.81 m/s^2; d_s is 1×10^{-2} m; ρ_s is 114.36 kg/m^3; C is 0.44; crushed straw is mostly in the form of long rods, so the correction factor is taken as 1.8. The above parameters are brought into Eq. (9) to Eq. (11) to obtain a suspension velocity v_{xm} of 3.82 m/s for the straw particle.

2.3.2 Conveying Airflow Velocity

During actual conveying, the conveying airflow velocity is maintained at 1.5-3 times the particle suspension velocity due to particle-particle collisions, particle-wall interactions, and non-uniform airflow distribution. To ensure experimental reliability, a conveying velocity of v_f = 1.7, $v_{xm} \approx$ 6.5 m/s is selected. CFD-DEM simulations at 6, 6.5, 7, and 8 m/s are conducted to validate the results. The simulation model and mesh structure of the conveying channel are illustrated in Fig. 4.

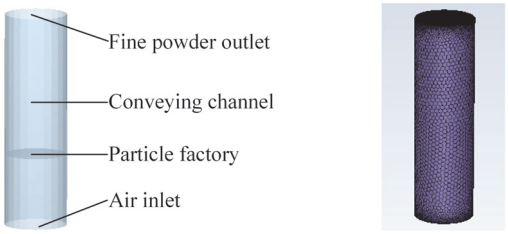

(a) Simulation model (b)Meshing

Figure 4 Simulation model and meshing of conveying channel: (a) Simulation model; (b) Meshing

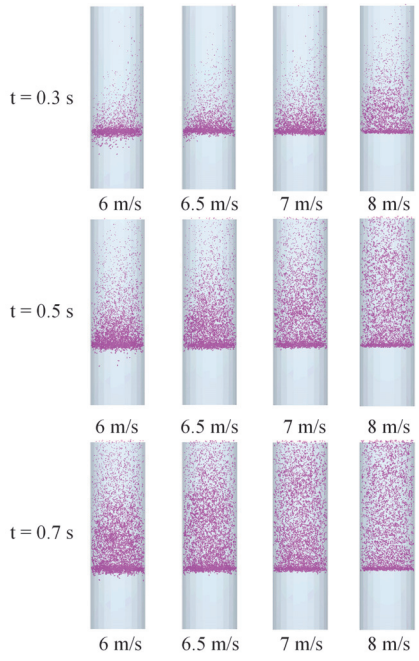

Figure 5 Simulation of conveying airflow velocity

Fig. 5 shows the movement of straw particles in the conveying channel at different conveying airflow velocities and at different times. At t = 0.3s, the tendency of the particles to rise is greater as the velocity increases. At velocities of 6 m/s and 6.5 m/s, the particles mostly pile up near the particle factory and even exhibit a tendency to fall; At t = 0.5 s, particles at all velocities begin to rise. In pipes with lower velocities, particles rise more slowly and continue to accumulate near the particle factory, while in pipes with higher velocities, particles rise uniformly; At t = 0.7 s, particles rise in all channels. In channels with lower velocities, the particles rise is uneven, leading to particle accumulation. In channels with higher velocities, the particle rise is more uniform. The above simulation results demonstrate that conveying airflow velocities of 6 m/s and 6.5 m/s are insufficient to sustain particle lift, potentially leading to clogging in the conveying channel. Conveying airflow velocities of 7 m/s and 8 m/s are sufficient to ensure continuous particle suspension and transport. Considering the principle of low power consumption, a conveying airflow velocity of 7 m/s is more suitable for conveying straw particles. Although the empirical formula suggests a conveying airflow velocity of 6.5 m/s, the final conveying air velocity is determined to be 7 m/s based on the simulation results.

2.3.3 Volumetric Flow Rate

The volumetric flow rate (Q) is a critical parameter influencing the straw conveying performance in pneumatic device. It can be calculated using Eq. (12). An optimal Q value reduces energy consumption while maintaining conveying efficiency [19].

$$Q = \frac{3600}{4} \pi D^2 v_f \tag{12}$$

where: Q is the volumetric flow rate / m^3/h, D is the equivalent diameter of the conveying channel / m, v_f is the conveying airflow velocity / m/s.

In accordance with the previous calculations, substituting v_f = 7m/s, D = 0.45 m into Eq. (12), the volumetric flow rate Q is obtained as 4007.87 m^3/h. Since the airflow pressure is lost in the conveying process, the actual volumetric flow rate is greater than 4007.87 m^3/h. The value of Q is taken as 4500 m^3/h.

2.4 Straw Conveying Process Simulation Experiment

The procedure of conveying straw by pneumatic conveying device is essentially the exchange of momentum and energy between the airflow and straw particles. The CFD-DEM can accurately simulate the interaction between airflow and straw particles, analyze factors such as airflow distribution and particle movement, and enhance the efficiency and stability of the conveying device [30].

(1) Model Simplification

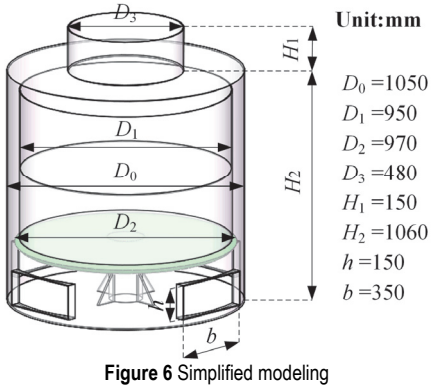

Figure 6 Simplified modeling

As shown in Fig. 6, the simplified model of the pneumatic conveying device mainly includes the air inlet, fine powder outlet, crushing hood, flow duiding loop, and flow deflector. This model is used for the subsequent fluid-solid coupling simulation of the straw conveying process.

(2) Grid Division

To preserve computational fluid continuity, this study employs Fluent Meshing for grid generation. Grids are primarily categorized into structured and unstructured types. When the model structure is geometrically complex, the grid shape becomes irregular, making structured grids unsuitable for robust solutions. In contrast, unstructured grids lack rigid topological relationships between elements, enabling effective handling of irregular domains. Therefore, this work adopts unstructured grids for discretization.

First, local sizing is applied to the structurally complex flow deflector to refine its grid. The surface grid is generated with a maximum element length of 35 mm and a minimum element length of 1.2 mm, along with 2 layers of gap-filling elements. The total number of generated grid elements is 553561, with a maximum skewness of 0.61 (values below 0.7 indicate good grid quality). Thus, the surface grid exhibits satisfactory quality and is suitable for subsequent volume grid generation. Given the complex internal geometry of the model, a poly-hexcore grid is adopted for volume filling. The maximum element size is set to 19.2 mm, while the minimum element size is 1.2 mm. The resulting grid consists of 3247793 elements, with a minimum orthogonal quality of 0.20 (values above 0.1 indicate acceptable volume grid quality). Thus, the volumetric grid demonstrates satisfactory quality for computational analysis. The average y+ value for near-wall grids is 95.44. The inclusion of boundary layers would compromise grid quality; therefore, to ensure computational convergence, boundary layers are not implemented. Fig. 7a illustrates the surface gridding results of the conveying device, while Fig. 7b demonstrates its corresponding volume gridding configuration.

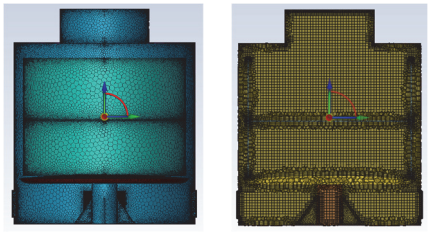

(a) Surface gridding (b)Volume gridding

Figure 7 Gridding of conveying device: (a) Surface meshing; (b) Volume gridding

(3) Configuration of Fluid Simulation Parameters and Boundary Conditions in Fluent

This study employs the commercial software ANSYS Fluent for numerical simulations. The governing equations consist of the continuity equation, momentum equation, and Navier-Stokes equations. The Reynolds number is obtained from Eq.(8) as 2.1×10^4. The RNG k-ε turbulence model is selected due to its superior adaptability and accuracy in simulating complex turbulent flows. This choice is made considering both the flow characteristics within the conveying device and the available computational resources. The specified boundary conditions and numerical discretization schemes are presented in Tab. 2. Furthermore, the steady-state solution obtained after 500 iterations serves as the initial condition for subsequent unsteady calculations.

Table 2 Boundary conditions and discretization schemes

Name	Condition
Air inlet	Velocity inlet
Fine powder outlet	Pressure-outlet:gauge pressure is 0 Pa
Wall	No slip
Turbulence intensity	3%
Pressure-velocity coupling	PISO
Pressure discretization	Second Order
Momentum discretization	Second Order Upwind
Turbulent kinetic energy	Second Order Upwind
Turbulent dissipation rate	Second Order Upwind

(4) Grid Independence Verification

Tab. 3 shows the selected mesh schemes. A grid independence study is conducted in this research by gradually reducing the grid element size or increasing the grid density. The airflow velocity at the air inlet is set to 6 m/s, and the average airflow velocity at the fine powder outlet is used as the criterion for grid independence evaluation.

Table 3 The number of grid cells

Simulation scheme number	The number of grid cells
1	1021242
2	1830441
3	2572416
4	3247793
5	3686232

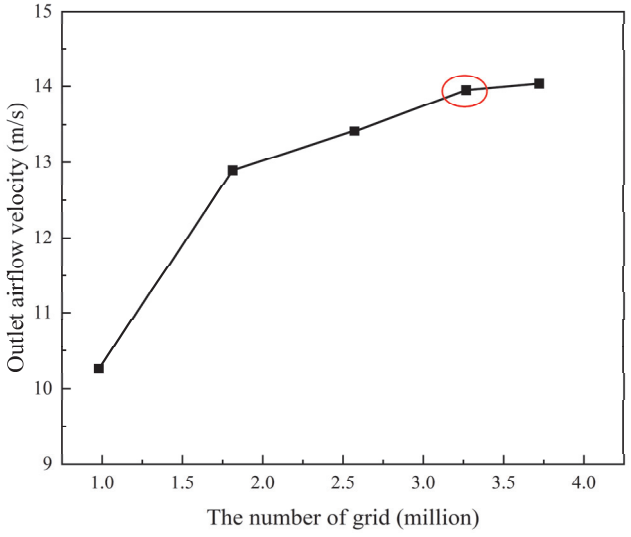

Figure 8 Grid independence verification results

As shown in Fig. 8, when the number of gridcells exceeds 3247793, the average airflow velocity at the fine powder outlet stabilizes, with a variation within 0.57%. Therefore, the grid scheme with 3247793 cells (Scheme 4) is selected for the subsequent simulation studies.

(5) Establishment and Parameter Setting of the Material Particle Model

The model parameter settings in EDEM mainly include the material property parameters and the mechanical parameters between the materials. The specific parameters are shown in Tab. 4 [31-33].

Table 4 Discrete element simulation parameters

Parameters	Values	Parameters	Values	Parameters	Values
Straw Density / kg/m^3	114.36	Density of conveying device / kg/m^3	7865	Normal stiffness per unit area / N/m^3	1.5×10^6
Straw Poisson ratio	0.3	Poisson ratio of conveying device	0.3	Shear stiffness per unit area / N/m^3	1×10^6
Straw Shear modulus / G/MPa	2.5	Shear modulus of conveying device / G/MPa	7.9×10^4	Normal range / N/m^3	30
Straw-straw Restitution coefficient	0.3	Restitution coefficient between straw and conveying device	0.45	Shear range / N/m^3	20
Straw-straw Static friction coefficient	0.5	Static friction coefficient between straw and conveying device	0.55	Normal strength / Pa	8.6×10^5
Straw-straw Rolling friction coefficient	0.15	Rolling friction coefficient between straw and conveying device	0.3	Shear strength / Pa	8.6×10^5

(6) Coupling Parameter Settings Between Fluent and EDEM

Considering the interaction forces between the airflow and straw particles, the coupling model adopts the Eulerian model. To ensure the computational stability and convergence of the CFD-DEM coupling simulation, the time step in FLUENT is set to 1×10^{-3} s, with 1500 time steps, resulting in a total simulation time of 1.5 s.

2.5 Performance Testing of Pneumatic Conveying Device

The prototype was manufactured based on the main structural design and parameter calculations of the pneumatic conveying device in the previous section. To verify whether the actual conveying capacity of the device meets the design requirements, a conveying performance test was conducted from January 14, 2024, to January 21, 2024, at the test site of the Engineering Training Center of Northeast Forestry University. Fig. 9 shows the test prototype and instruments used during the testing process: Fig. 9a is the ZFJ-II standard test sieve machine (20-mesh sieve); Fig. 9b is the single-phase AC electronic regulator (4 kW regulator power); Fig. 9c is the rapid moisture meter (accuracy 0.01%); Fig. 9d is the thermal anemometer (range 30 m/s, accuracy 0.01 m/s); Fig. 9e is the electronic scale (range 200 kg, accuracy 0.01 kg); Fig. 9f is the test prototype; Fig. 9g is the vernier scale (range 150 mm, accuracy 0.01 mm).

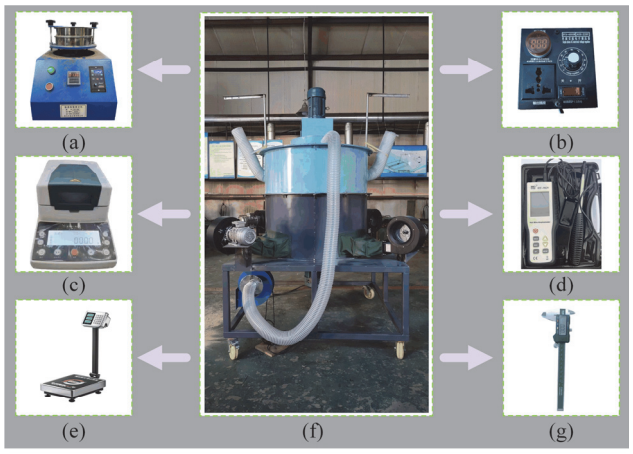

Figure 9 Test prototypes and instruments: (a) ZFJ-II standard test sieve machine; (b) Single-phase AC electronic regulator; (c) Rapid moisture meter; (d) Thermal anemometer; (e) Electronic scale; (f) Test prototype; (g) Vernier scale

The harvested corn stalks are crushed in a coarse crusher and sifted to remove broken stalks and impurities by using a sifter. The average length of the straw is measured as 10 mm and the moisture content is 20.16%. Since the performance test is conducted only for the pneumatic conveying device, the crushing motor and the classifying motor are shut down during the test. The rotation speed of the ventilators is regulated by electronic voltage regulators. A thermal anemometer measures the inlet airflow velocity. When the inlet airflow velocity is stabilized at 8.4 m/s, the test straw is put into the screw conveyor, the discharging time is recorded with a stopwatch, and the mass of collected straw is measured by an electronic scale. To ensure the reliability of the test results, the test is repeated eight times.

3 RESULT AND DISCUSSION

3.1 Analysis of Straw Conveying Process Simulation Results

To observe the motion characteristics of airflow and straw particles in the conveying device, six cross-sections are selected as observation surfaces. Based on the gas-solid coupling method, the distribution of the airflow and the motion state of strawparticles at different moments in the conveying device are investigated to provide a theoretical basis for determining the key parameters of the conveying device.

A very complex airflow field exists inside the conveying device during straw conveying, and different results are observed at different observation positions. To facilitate observation of the airflow trajectory and characteristics inside the conveying device, six observation planes are selected and labeled C_1-C_6, as shown in Fig. 10.

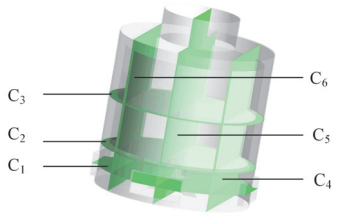

Figure 10 Election of observation planes

3.1.1 Airflow Distribution Patterns in the Conveying Device

When analyzing the airflow inside the conveying device, the air inlet width b is 350 mm, the air inlet height h is 150 mm, and the inlet airflow velocity is 6 m/s. Fig. 11 presents the velocity contours on observation planes C_1- C_6 within the conveying device.

At observation plane C_1, the central region exhibits the minimum airflow velocity. Non-uniform airflow distribution is observed between the air inlets, attributed to airflow divergence within the air storage chamber leading to velocity decay. At observation plane C_2, upon passing through the annular gap between the flow deflector and conveying channel, the airflow velocity increases significantly due to flow area contraction. In most areas, the airflow velocity exceeds 7 m/s, but the airflow velocity distribution remains uneven. The airflow velocity above the air inlets is markedly higher than in non-inlet areas. Simulated optimization of air inlet sizes is required. At observation plane C_3, the average airflow velocity is 6.78 m/s. The airflow velocity on the outside of the conveying channel is higher than on the inside. The observed flow behavior results from the flow deflector's outer diameter exceeding the conveying channel's inner diameter, which creates a flow obstruction that prevents axial airflow development along the channel wall. This geometric constraint necessitates optimization of the flow deflector diameter to improve flow characteristics.

Since observation planes C_4 and C_6 are symmetric with respect to observation plane C_5, the airflow motion characteristics on these two planes are consistent. By analyzing the airflow distribution map (Fig. 11c) and the airflow field vector map (Fig. 12) at observation plane C_5, the following observations can be made: The airflow velocity declines as it fills the entire air storage chamber and then surges as it passes through the gap between the flow deflector and conveying channel. The airflow velocity inside the crushing chamber is low, which indicates that the airflow in the conveying channel does not affect the internal airflow field of the crushing chamber and further verifies the feasibility of the structure of the flow deflector. At the top of the conveying device, the airflow appears uneven, suggesting that a transition structure should be provided. The presence of vortices in the classifying chamber is due to the coherent structure of the airflow due to the special structure of the conveying device. Vortices are also present in the air storage chamber; however, since the air storage chamber does not participate in particle transportation, it does not affect the conveying process.

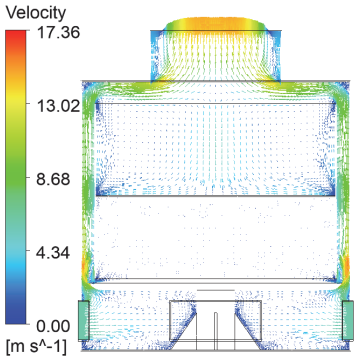

Figure 12 Airflow field vector map inside the conveying device

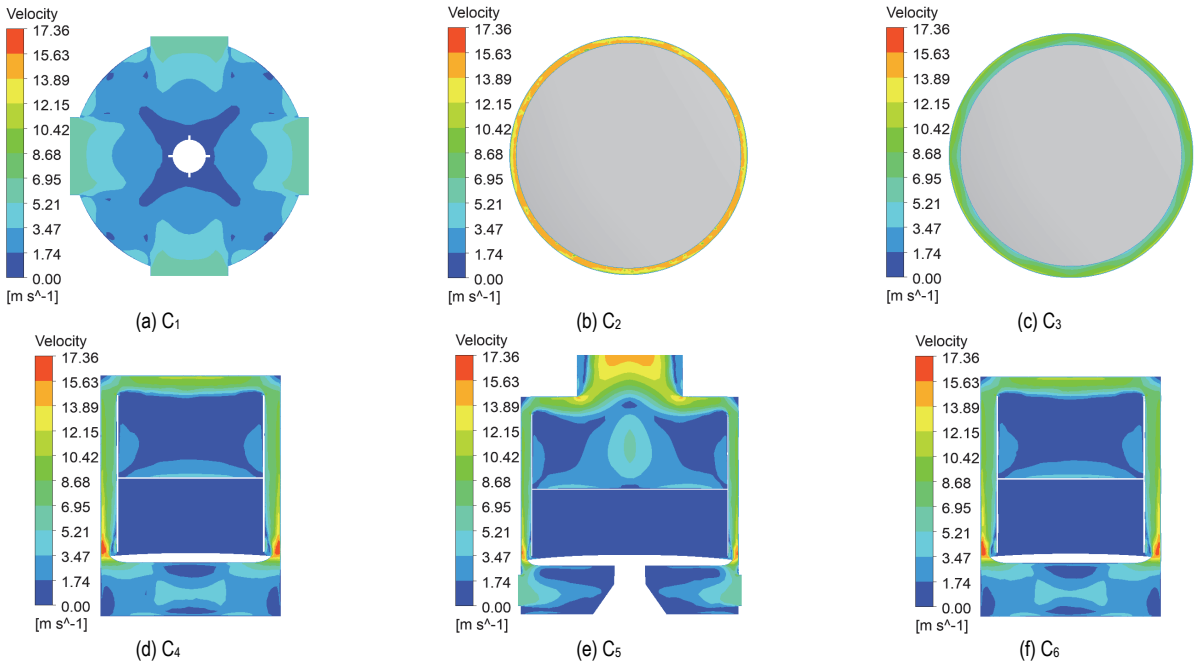

Figure 11 Airflow distribution inside the conveying device

3.1.2 Analysis of Straw Particle Motion Characteristics

When examining straw particles inside the conveying device, the air inlet width b is 350 mm, the air inlet height h is 150 mm, the inlet airflow velocity is 6 m/s, and the particle feed rate is 600 kg/h. Fig. 13 illustrates the motion characteristics of straw particles at different time instants.

At t = 0.00 s, the particles are generated at a rate of 0.17 kg/s and fall under the force of gravity. At t = 0.18 s, some particles reach the flow deflector and begin to accumulate. At t = 0.29 s owing to the inclination and constant rotation of the upper surface of the flow deflector, some particles leave the crushing chamber and enter the conveying channel under the action of centrifugal force and gravity. At t = 0.5 s, particles in the conveying channel accelerate upward with the airflow to the top of the conveying device, with a few particles falling into the classifying chamber. At t = 0.75 s, a large number of particles reach the top of the conveying device. However, due to the obstruction at the upper part of the device, the rising speed of particles decreases noticeably. The straw particles briefly accumulate before entering the classifying

chamber with the airflow. At $t = 1.00$ s, most straw particles gathered at the top of the conveying device fall into the crushing chamber, while others exit through the fine powder outlet. The results demonstrate that the conveying device can effectively transport straw particles from the crushing chamber to the classifying chamber and fine powder outlet under the current operating conditions.

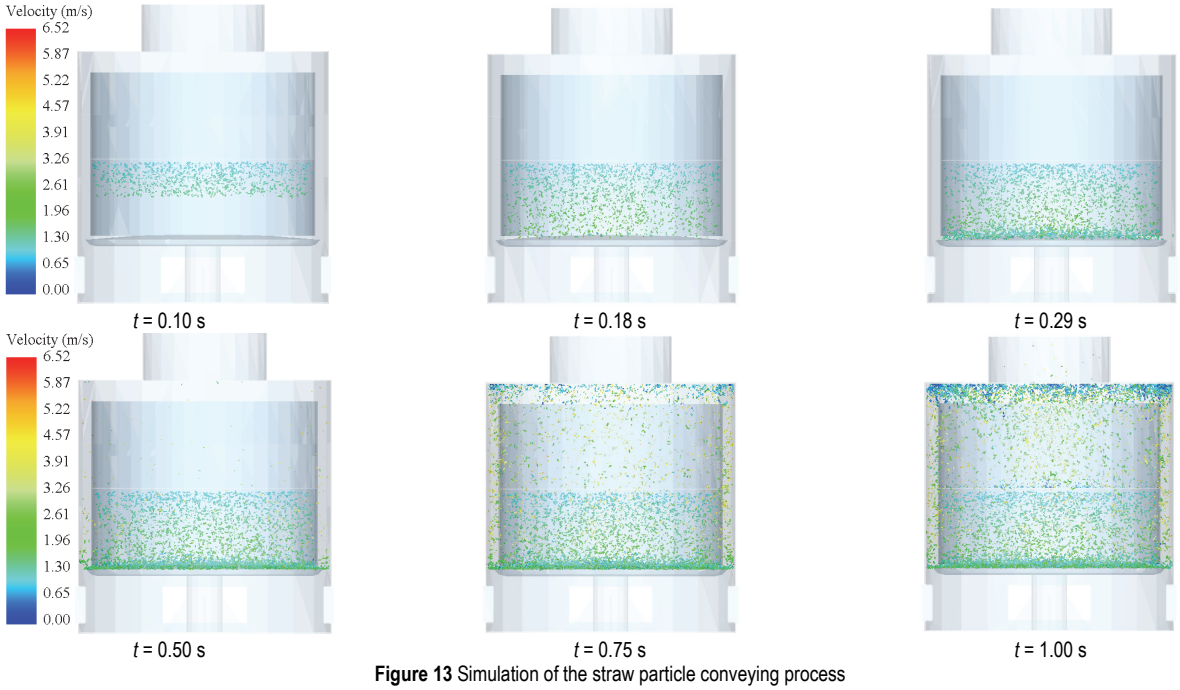

Figure 13 Simulation of the straw particle conveying process

3.2 Effects of Structural and Working Parameters of Conveying Device on Conveying Efficiency

This section examines how three parameters (air inlet width, inlet airflow velocity, and flow deflector diameter) influence conveying efficiency, based on prior theoretical and simulation analyses.

3.2.1 Effect of Air Inlet Width on Conveying Efficiency

Increasing the air inlet width improves airflow uniformity within the conveying channel. However, the housing design imposes an upper limit of 350 mm on the air inlet width. Herein, we evaluate the impact of three distinct air inlet widths (150 mm, 250 mm, and 350 mm) on conveying efficiency. In the study of the Influence of air inlet width on conveying efficiency, the structure and dimensions of the conveying channel remain unchanged, ensuring that the internal airflow velocity is related to the total airflow volume. To control a single variable and ensure consistent airflow volumes, the inlet area and airflow rate are varied. For the simulation, the inner diameter of the conveying channel is 950 mm, the outer diameter is 1050 mm, and the inlet airflow velocities are 14 m/s, 8.4 m/s, and 6 m/s, respectively.

Fig. 14 presents the average airflow velocity at observation plane C_2, and Fig. 15 presents the average airflow velocity at observation plane C_3. From Fig. 14 and Fig. 15, it is evident that when the air inlet width is 150 mm, the airflow distribution in the conveying channel is highly uneven, potentially causing material to accumulate as it rises in the channel. As the air inlet width increases to 350 mm, the airflow in the conveying channel becomes uniform, significantly reducing the likelihood of material accumulation.

A comparison of energy consumption parameters and velocity gradient volume averages at observation plane C_1 for the three air inlet widths are presented in Tab. 5 and Tab. 6. As the air inlet width increases, the turbulent kinetic energy and turbulent dissipation rate increase, while the maximum velocity and turbulent energy spectrum decrease. The lateral velocity gradient decreases as the air inlet width increases, which is not favorable for straw transport. In summary, the optimal air inlet width is determined to be 250 mm.

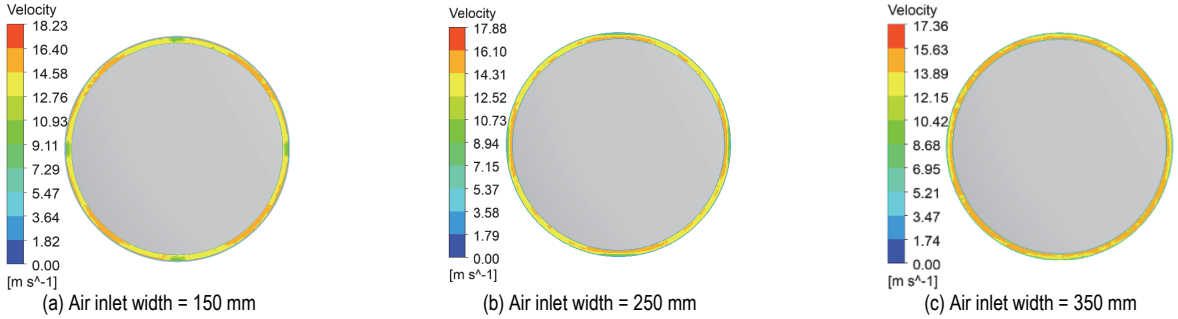

(a) Air inlet width = 150 mm (b) Air inlet width = 250 mm (c) Air inlet width = 350 mm

Figure 14 Airflow velocity distribution at observation plane C_2

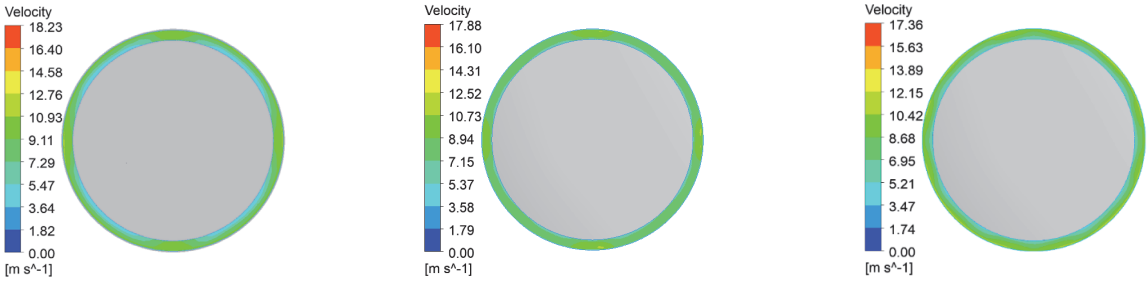

(a) Air inlet width = 150 mm (b) Air inlet width = 250 mm (c) Air inlet width = 350 mm

Figure 15 Airflow velocity distribution at observation plane C_3

Table 5 Energy consumption parameters for different air inlet widths

Air inlet width / mm	Maximum velocity / m/s	Turbulent kinetic energy / m^2/s^2	Turbulent dissipation rate / m^2/s^3	Turbulence energy Spectra
150	18.26	0.86	368.62	65.43
250	17.88	1.62	416.48	62.19
350	17.36	1.98	696.76	48.37

Table 6 Average value of velocity gradient under different air inlet widths

Air inlet width / mm	Transverse velocity gradient / s^{-1}	Longitudinal velocity gradient / s^{-1}
150	18.26	1.018
250	17.67	1.274
350	17.36	1.665

3.2.2 Effect of Inlet Airflow Velocity on Conveying Efficiency

The inlet airflow velocity significantly influences both updraft velocity and straw particle trajectories within the conveying channel, affecting overall conveying efficiency. When the air inlet width is 250 mm, the inlet airflow velocity is calculated as 8.4 m/s using Eq. (12). According to the calculation results in Section 2.3, the minimum updraft velocity required to support the upward movement of straw particles is 6 m/s. Substituting this into Eq. (1) and Eq. (12) gives an inlet airflow velocity of 7.2 m/s. To maintain the required volumetric flow rate of 4500 m^3/h, a 750 W ventilator is selected. The maximum volumetric flow rate of the ventilator is 1450 m^3/h. Substituting 1450 m^3/h into Eq. (12) gives an inlet airflow velocity of 10 m/s. This section systematically examines the impact of inlet airflow velocity on conveying efficiency at three distinct levels: 7.2 m/s, 8.4 m/s, and 10 m/s.

Fig. 16 shows the airflow velocity distribution at observation plane C_2 when the inlet airflow velocities are 7.2 m/s, 8.4 m/s, and 10 m/s, respectively. As shown in Fig. 16a, when the inlet airflow velocity is 7.2 m/s, the average airflow velocity at observation plane C_2 is 12.77 m/s. As shown in Fig. 16b, when the inlet airflow velocity is 8.4 m/s, the average airflow velocity at observation plane C_2 is 14.02 m/s. As shown in Fig. 16c, when the inlet airflow velocity is 10 m/s, the average airflow velocity at observation plane C_2 is 17.47 m/s. The three average airflow velocities mentioned above are all greater than the suspension velocity of straw particle, meeting the transportation conditions for the straw. However, the airflow velocity on the inner side of the conveying channel is significantly higher than that on the outer side, which will cause most of the straw to be pushed to one side of the conveying channel, thereby reducing the conveying efficiency.

Fig. 17 shows the airflow velocity distribution at observation plane C_3 when the inlet airflow velocities are 7.2 m/s, 8.4 m/s, and 10 m/s, respectively. The airflow distribution is the most uniform when the inlet airflow velocity is 8.4 m/s. When the inlet airflow velocity is 7.2 m/s, the airflow distribution is the least uniform.

When the inlet airflow velocity is too low, the airflow within the transport channel is insufficient to smoothly convey all the particles upwards, and the straw particles may accumulate at certain locations. When the inlet airflow velocity is too high, the upward movement speed of the straw particles increases, but insufficient particles are transported upward in the conveying channel, leading to reduced conveying efficiency and increased energy consumption per unit. The energy consumption parameters at observation plane C_1 are compared for three inlet airflow velocities, as shown in Tab. 7. As the inlet velocity grows, the turbulent kinetic energy of the flow field in the conveying channel rises and the turbulent energy spectrum decreases, the effective energy utilization is reduced. At the same time, the turbulent dissipation rate increases, the maximum negative pressure grows, and the maximum linear velocity reduces. In summary, the inlet airflow velocity is determined to be 8.4 m/s.

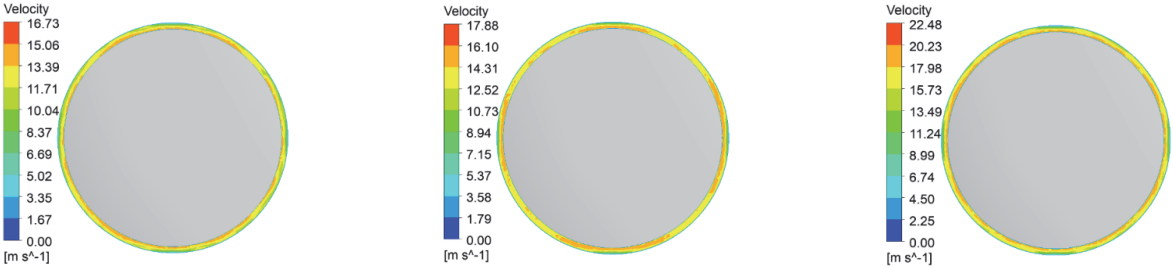

(a) Inlet airflow velocity = 7.2 m/s (b) Inlet airflow velocity = 8.4 m/s (c) Inlet airflow velocity = 10 m/s

Figure 16 Airflow velocity distribution at observation plane C_2

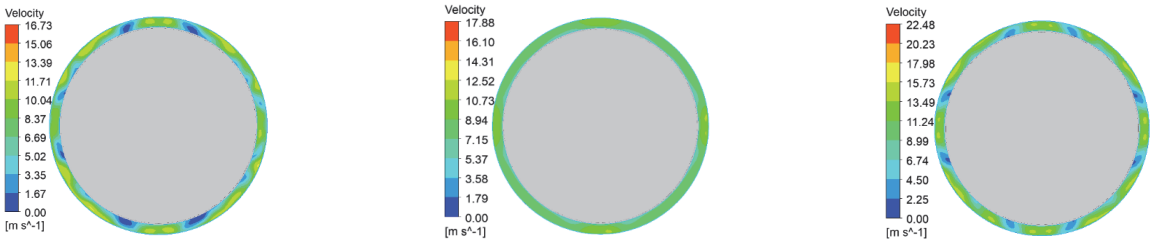

(a) Inlet airflow velocity = 7.2 m/s (b) Inlet airflow velocity = 8.4 m/s (c) Inlet airflow velocity = 10 m/s

Figure 17 Airflow velocity distribution at observation plane C_3

Table 7 Energy consumption parameters under different inlet airflowvelocities

Inlet airflow velocity / m/s	Maximum velocity / m/s	Turbulent kinetic energy / m^2/s^2	Turbulent dissipation rate / m^2/s^3	Turbulence Energy Spectra
7.2	16.73	0.94	303.50	68.21
8.4	17.88	1.62	416.48	62.19
10	22.48	3.12	683.26	57.63

3.2.3 Effect of Flow Deflector Diameter on Conveying Efficiency

As established in Section 3.1, the flow deflector diameter directly modifies both the conveyance channel geometry and airflow dynamics, significantly impacting the fluid-particle interaction. A reduction in flow deflector diameter correlates with diminished influence on airflow uniformity. However, when the flow deflector diameter is too small, its ability to isolate and deflect the airflow is reduced. In accordance with the size of the conveying channel, the range of flow deflector diameter is 970-1010 mm. Thus, this section investigates the effect on conveying efficiency when flow deflector diameter is 970 mm, 990 mm, and 1010 mm, respectively.

Fig. 18 shows the airflow velocity clouds at the observation plane C_5 for different flow deflector diameters. With an increase in the flow deflector diameter, the distribution of airflow at the gap between the flow deflector and conveying channel becomes more uneven. When the flow deflector diameter is 970 mm, the range of the airflow velocity at the gap between the flow deflector and conveying channel is smaller, and the flow field is more stable. However, the intensity of the vortex in the classifying chamber is high, which affects the classifying efficiency. When the flow deflector diameter is 990 mm, the vortex intensity at the air inlet increases. The span of the airflow velocity at the gap between the flow deflector and conveying channel increases, and the stability of the flow field deteriorates. Nevertheless, the intensity of the vortex in the classifying chamber decreases, reducing its effect on classification. When the flow deflector diameter is 1010 mm, the vortex strength at the air inlet increases further. The range of the airflow velocity at the gap between the flow deflector and conveying channel increases, and the stability of the flow field decreases. The intensity of eddy currents in the classifying chamber decreases, reducing their effect on classification. However, the airflow velocity at the fine powder outlet decreases, which hinders the collection of materials after classification.

Fig. 19 shows the airflow velocity clouds at observation plane C_2 for different flow deflector diameters. When the flow deflector diameter is 970 mm, the airflow velocity in some areas is lower than the suspension velocity of straw particle, preventing their conveyance. Therefore, the flow deflector diameter must not be too small.

Fig. 20 shows the airflow velocity clouds at observation plane C_3 for different flow deflector diameters. The average airflow velocities in Fig. 20a to Fig. 20c are 7.66 m/s, 7.54 m/s, and 7.22 m/s, respectively, all of which exceed the minimum velocity required for upward conveying of the particles, making them sufficient for conveying straw particles.

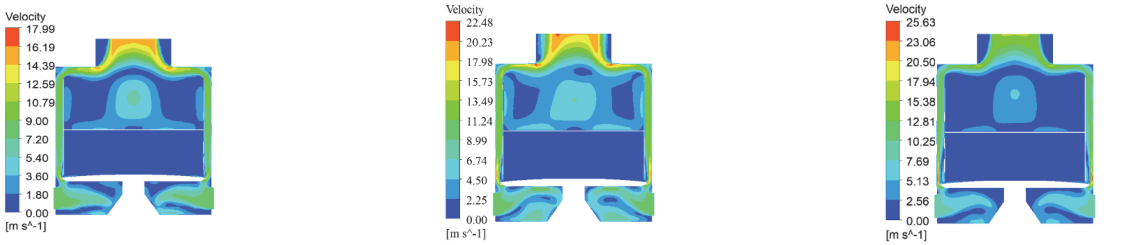

(a) Flow deflector diameter = 970 mm (b) Flow deflector diameter= 990 mm (c) Flow deflector diameter = 1010 mm

Figure 18 Comparison of airflow velocity clouds at observation plane C_5

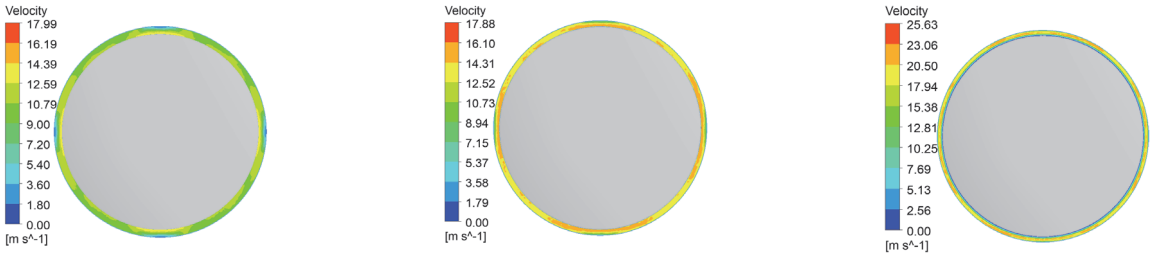

(a) Flow deflector diameter = 970 mm (b) Flow deflector diameter = 990 mm (c) Flow deflector diameter = 1010 mm

Figure 19 Comparison of airflow velocity clouds at observation plane C_2

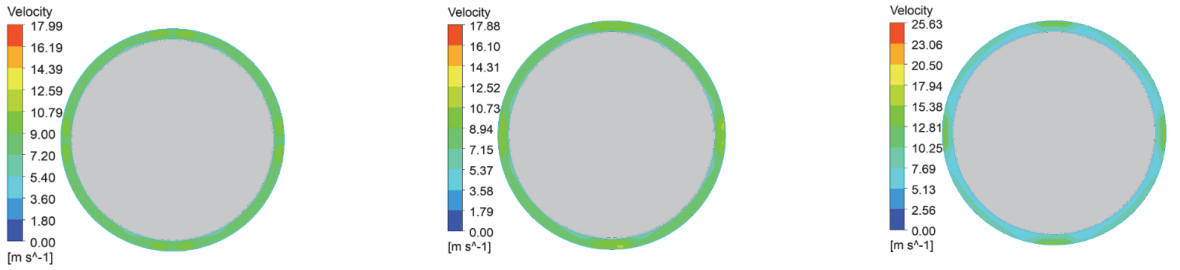

(a) Flow deflector diameter = 970 mm (b) Flow deflector diameter = 990 mm (c) Flow deflector diameter = 1010 mm

Figure 20 Comparison of airflow velocity clouds at observation plane C_3

3.3 Experimental Results and Analysis of Conveying Performance

The actual conveying capacity G_s of the test device is calculated by Eq. (13).

$$G_S = \frac{M}{t} \tag{13}$$

where: M is the weight of straw to be conveyed / kg; t is the discharging time / s.

The relative error δ in conveying capacity is calculated from Eq. (14).

$$\delta = \frac{|G_s - G_t|}{G_t} \cdot 100\% \tag{14}$$

where: G_t is the theoretical conveying capacity / kg/h, G_s is the actual conveying capacity / kg/h.

The collected straw is shown in Fig. 21. The test results of the conveying capacity are shown in Tab. 8. The relative errors of the conveying capacity of this test device are all less than 5.88%, and the errors are less than 10% [34], indicating that this test device can meet the design requirements of the theoretical conveying capacity.

Figure 21 The collected straw

Table 8 Results of conveying performance tests

No.	M / kg	t / s	G_s / kg/h)	G_t / kg/h	δ / %
1	10	51	705.88	750	5.88
2	10	50	720.00	750	4.00
3	10	49	734.69	750	2.04
4	10	47	765.96	750	2.13
5	20	99	727.27	750	3.03
6	40	199	723.62	750	3.52
7	45	215	753.49	750	0.47
8	80	386	746.11	750	0.52

4 CONCLUSIONS

(1) To effectively address the critical issue of low material conveying efficiency in traditional impact crushers caused by complex internal flow field interactions, this study developed a pneumatic conveying system for straw micro-pulverization. The core innovation lies in decoupling the three key processes - crushing, conveying, and classifying - into functionally independent working zones, which fundamentally eliminates cross-process interference and significantly enhances overall system performance.

(2) The application of CFD-DEM coupled numerical simulation provided deeper insights beyond conventional empirical approaches, yielding three significant findings that are difficult to obtain through prototype testing: (i) Quantitative analysis revealed the correlation between airflow velocity and particle suspension state, identifying 7 m/s as the optimal conveying airflow velocity that minimizes energy consumption while preventing straw particle deposition; (ii) Simulation results elucidated the regulatory effects of geometric parameters (250 mm air inlet width, 990 mm flow deflector diameter) and operational parameters (8.4 m/s inlet airflow velocity) on airflow uniformity within the conveying device, which directly determine the stability and efficiency of straw particle transport; (iii) Precise identification of detrimental vortex structures in the classifying chamber and air storage chamber - phenomena extremely challenging to diagnose experimentally - provided clear direction for future structural optimization.

(3) Performance evaluation based on the relative error of conveying capacity demonstrated that the device achieved a relative error below 5.88% with no material adhesion or clogging in the conveying channel. The device operated stably and reliably. These test results validated the rationality of the pneumatic conveying device's structural design and confirmed the accuracy of both theoretical calculations and CFD-DEM coupled simulation results.

Acknowledgements

This research was funded by the National Science Foundation of China (Grant No. 51975114).

5 REFERENCES

[1] Koul, B., Yakoob, M., & Shah, M. P. (2021). Agricultural waste management strategies for environmental sustainability. *Environmental Research*, *206*, 112285. https://doi.org/10.1016/j.envres.2021.112285

[2] Rossi, G., Conti, L., Fiorineschi, L., Marvasi, M., Monti, M., Rotini, F., Togni, M., & Barbari, M. (2020). A new eco-friendly packaging material made of straw and bioplastic. *Journal of Agricultural Engineering*, *51*(4), 185-191. https://doi.org/10.4081/jae.2020.1088

[3] Zhang, S. (2019). Study on the preparation process of rice straw fiberboard for packaging. *IOP Conference Series Earth and Environmental Science*, *233*, 052031. https://doi.org/10.1088/1755-1315/233/5/052031

[4] Dahy, H. (2017). Efficient fabrication of sustainable building products from annually generated non-wood cellulosic fibres and bioplastics with improved flammability resistance. *Waste and Biomass Valorization*, *10*(5), 1167-1175. https://doi.org/10.1007/s12649-017-0135-3

[5] Fu, Y., Zhang, J., & Guan, T. (2023). High-Value utilization of corn straw: From waste to wealth. *Sustainability*, *15*(19), 14618. https://doi.org/10.3390/su151914618

[6] Gu, Y. M., Kim, S., Sung, D., Sang, B., & Lee, J. H. (2019). Feasibility of continuous pretreatment of corn stover: A comparison of three commercially available continuous pulverizing devices. *Energies*, *12*(8), 1422. https://doi.org/10.3390/en12081422

[7] Li, W., Shao, Y., Zhu, J., Zhang, H., & Zhang, H. (2018). Reducing comminution over-grinding of powder coatings with modified grinding pins in an air classifier mill. *Powder Technology*, *344*, 36-45. https://doi.org/10.1016/j.powtec.2018.11.076

[8] Yan, X., Liu, C., Huang, A., Chen, R., Chen, J., & Luo, S. (2020). The nutritional components and physicochemical properties of brown rice flour ground by a novel low temperature impact mill. *Journal of Cereal Science*, *92*, 102927. https://doi.org/10.1016/j.jcs.2020.102927

[9] Kuang, S., Zhou, M., & Yu, A. (2019). CFD-DEM modelling and simulation of pneumatic conveying: A review. *Powder Technology*, *365*, 186-207. https://doi.org/10.1016/j.powtec.2019.02.011

[10] Yan, L., Wang, N., & Xu, Z. (2022). Experimental study on the effectiveness and safety of cement powder on extinguishing metal magnesium fires based on pneumatic conveying technology. *Case Studies in Thermal Engineering*, *37*, 102279. https://doi.org/10.1016/j.csite.2022.102279

[11] Sheng, L., Xiao, Y., Hsiau, S., Chen, C., Lin, P., & Jen, K. (2020). A study of pneumatic conveying with high-density AM-using metal powder in a pipe bend. *International Journal of Mechanical Sciences*, *181*, 105763. https://doi.org/10.1016/j.ijmecsci.2020.105763

[12] Olaleye, A. K., Shardt, O., Walker, G. M., & Van Den Akker, H. E. (2019). Pneumatic conveying of cohesive dairy powder: Experiments and CFD-DEM simulations. *Powder Technology*, *357*, 193-213. https://doi.org/10.1016/j.powtec.2019.09.046

[13] Zhang, F., Olaleye, A. K., O'Mahony, J. A., Miao, S., & Cronin, K. (2020). Dilute phase pneumatic conveying of whey protein isolate powders: Particle breakage and its effects on bulk properties. *Advanced Powder Technology*, *31*(8), 3342-3350. https://doi.org/10.1016/j.apt.2020.06.019

[14] Xu, H., Gao, J., Zhong, W., & Zhu, H. (2021). Experimental study on the fluidization discharging characteristics of Geldart-C kaolin powders in a blow tank with pulsed gas. *Advanced Powder Technology*, *33*(1), 103372. https://doi.org/10.1016/j.apt.2021.11.024

[15] Chen, L., Sun, Z., Ma, H., Pan, G., Li, P., & Gao, K. (2022). Flow characteristics of pneumatic conveying of stiff shotcrete based on CFD-DEM method. *Powder Technology*, *397*, 117109. https://doi.org/10.1016/j.powtec.2022.117109

[16] Jägers, J., Brömmer, M., Illana, E., Wirtz, S., & Scherer, V. (2021). DEM-CFD simulation of wood pellet degradation by particle-wall impact during pneumatic conveying. *Powder Technology*, *391*, 385-402. https://doi.org/10.1016/j.powtec.2021.06.037

[17] Markauskas, D., Platzk, S., & Kruggel-Emden, H. (2022). Comparative numerical study of pneumatic conveying of flexible elongated particles through a pipe bend by DEM-CFD. *Powder Technology*, *399*, 117170. https://doi.org/10.1016/j.powtec.2022.117170

[18] Lu, H., Chen, M., Guo, X., Liu, H., & Gong, X. (2021).Dense phase pneumatic conveying of pulverized coal in industry-scale vertical pipeline. *Chemical Engineering (CHINA)*, *49*(2), 45-49.

[19] Zhou,J., Guo, X., Ba, H., Li, B., & Liu, X. (2023).Study of Flow Pattern for Vertical Pipe Pneumatic Conveying by CFD-DEM Coupled Simulation. *Journal of Engineering Thermophysics*, *44*(9), 2464-2473.

[20] Song, J., Wang, T., Hu, G., Zhang, Z., Zhao, W., Wang, Z., & Zhang, Y. (2023). Conveying characteristics of shrimp feed pellets in pneumatic conveying system and minimum power consumption dissipation factor. *Aquacultural Engineering*, *102*, 102347. https://doi.org/10.1016/j.aquaeng.2023.102347

[21] Chen, L., Ma, H., Gao, K., & Sun, Z. (2023). Experimental study on the flow characteristics of horizontal pneumatic conveying of stiff shotcrete. *Journal of Building Engineering*, *73*, 106765. https://doi.org/10.1016/j.jobe.2023.106765

[22] Wang, C., Li, W., Li, B., Jia, Z., Jiao, S., & Ma, H. (2023). Study on the influence of different factors on pneumatic conveying in horizontal pipe. *Applied Sciences*, *13*(9), 5483. https://doi.org/10.3390/app13095483

[23] Fu, M., Gao, Z., Wang, C., Zhan, M., & Cao, Z. Structure design and pulverizing performance numerical simulation of straw micro-pulverizing cutter. *Renewable Energy Resources*, *42*(10), 1279-1288.

[24] Qin, M., Jin, Y., Cao, M., Wu, F., Luo, W., Guo, K., Xu, H., Gu, F., & Hu, Z. (2023). Design and parameter optimization of a Negative-Pressure peanut Fruit-Soil separating device. *Agronomy*, *13*(9), 2338. https://doi.org/10.3390/agronomy13092338

[25] Fu, P., Liu, L., Yang, W., Liu, R., Zhang, K., Guo, W., & Leng, C. (2021). Design and test of feed pneumatic conveying system. *Heilongjiang Animal Science and Veterinary Medicine*, *24*, 76-82.

[26] Yatskul, A. & Lemiere, J. (2017). Establishing the conveying parameters required for the air-seeders. *Biosystems Engineering*, *166*, 1-12. https://doi.org/10.1016/j.biosystemseng.2017.11.001

[27] Wang, F., Yang, G., Ke, W., & Ma, S. (2018). Studies on suspension property of sugarcane components. *IFAC-PapersOnLine*, *51*(17), 526-531. https://doi.org/10.1016/j.ifacol.2018.08.155

[28] Wen, X., Jia, H., Zhang, S., Yuan, H., Wang, G., & Chen, T. (2020). Test of suspension velocity of granular fertilizer based on EDEM-Fluent coupling. *Transactions of the Chinese Society for Agricultural Machinery*, *51*(3), 69-77.

[29] Zhu, Z., Kang, M., Liu, K., Ma, W., & Shen, X. (2022). Theoretical Calculation and Experimental Study on Suspension Velocity of Walnut and Its Main Components after Mechanical Shell Cracking. *Journal of Sichuan Agricultural University*, *40*(4), 610-618.

[30] Ren, D., Yu, H., Zhang, R., Li, J., Zhao, Y., Liu, F., Zhang, J., & Wang, W. (2022). Research and experiments of hazelnut harvesting machine based on CFD-DEM analysis. *Agriculture*, *12*(12), 2115. https://doi.org/10.3390/agriculture12122115

[31] Fu, M., Chen, X., Gao, Z., Wang, C., Xu, B., & Hao, Y. (2023). PARAMETERS CALIBRATION OF DISCRETE ELEMENT MODEL FOR CRUSHED CORN STALKS. *INMATEH Agricultural Engineering*, 399-408. https://doi.org/10.35633/inmateh-69-37

[32] Fu, M., Zhan, M., Cao, Z., Chen, L., Gao, Z., & Chen, X. (2024). Design and test of an airfoil crushing chamber for the

straw micro-crusher. *Journal of Mechanical Science and Technology*, *38*(11), 6097-6111. https://doi.org/10.1007/s12206-024-1027-7

[33] Wilczyński, D., Wałęsa, K., Talaśka, K., & Wojtkowiak, D. (2023). Experimental study on the mechanical behavior of dry corn stalk cutting. *Materials*, *16*(8), 3039. https://doi.org/10.3390/ma16083039

[34] Fang, X., An, H., Liu, Z., Li, Y., Feng, Z., Peng, B., & Wang, Y. (2020). Experimental research on pressure drop in dense phase pneumatic conveying of pulverized coal blending extract residue of direct coal liquefaction residue. *Journal of China Coal Society*, *45*(4), 1510-1518.

Contact information:

Min FU, PhD, Professor
(Corresponding author)
College of Mechanical and Electrical Engineering,
Northeast Forestry University,
Harbin Heilongjiang, 150040, China
E-mail: fumin@nefu.edu.cn

Lei CHEN
College of Mechanical and Electrical Engineering,
Northeast Forestry University,
Harbin Heilongjiang, 150040, China
E-mail: 18642102190@163.com

Zhong CAO
College of Mechanical and Electrical Engineering,
Northeast Forestry University,
Harbin Heilongjiang, 150040, China
E-mail: caozhong1023@163.com

Mingyu ZHAN
College of Mechanical and Electrical Engineering,
Northeast Forestry University,
Harbin Heilongjiang, 150040, China
E-mail: 13644681087@163.com

Zijian WANG
College of Mechanical and Electrical Engineering,
Northeast Forestry University,
Harbin Heilongjiang, 150040, China
E-mail: t15245987049@163.com